

Environmental Conditions Associated with Observed Snowband Structures within Northeast U.S. Winter Storms

Sara A. Ganetis¹, Brian A. Colle¹, Sandra E. Yuter² and Nicole P. Hoban²

¹School of Marine and Atmospheric Sciences, Stony Brook University / SUNY,

Stony Brook, New York

² Department of Marine, Earth, and Atmospheric Sciences, North Carolina State University,

Raleigh, North Carolina

For submission to *Monthly Weather Review*

12 February 2017

Revised: 28 June 2018

Second Revision: 29 August 2018

15

16

17

18

20

22

23
24

24
25

25
26

26 Email: ofran.come@stonybrook.edu

26 Email: brian.cone@stonybrook.edu

27

Abstract

Northeast U.S. winter storms commonly exhibit multiple meso- β scale ($L < 200$ km) bands of enhanced radar reflectivity and precipitation. We use radar observations, upper air soundings, and reanalyses from 108 cases of cool-season (Oct–Apr) storms from 1996–2016 that occurred within the coastal corridor from Delaware to Maine to identify and assess various banding structures and environments. Banding can occur in several configurations among storms, and banding characteristics can differ at different times within the same storm. We classified 6-hour storm periods as containing long (> 200 km) single bands, single bands co-occurring with sets of mesoscale multi-bands, multi-bands only, and radar echoes without any bands using a combination of automated and manual methods. Use of radar reflectivity data at 0.5 dB precision and a variable rather than a fixed threshold showed that the occurrence of long single bands without any mesoscale multi-bands was rare occurring in only 5 of 113 6-h periods. The most frequently occurring band configuration (55%) was concurrent single bands and multi-bands, which usually were present in the northwest quadrant of mature cyclones. Sets of multi-bands without a nearby single band usually occurred in the northeast quadrant of a cyclone poleward of weak-midlevel forcing along a warm front. Overall, mesoscale single and multi-bands more commonly occurred after the cyclone occluded than in the developing stages. Multi-bands occurred in a wide range of frontogenesis and moist potential vorticity environments.

45

46

47 **1. Introduction**

48 Mesoscale banding within United States (U.S.) East Coast winter storms can lead to
49 localized heavy snowfall rates and accumulations that can negatively impact lives and property
50 within the heavily populated urban corridors of the Mid-Atlantic and New England states. For
51 example, the recent blizzard of 8–9 February 2013 exhibited an intense mesoscale snowband and
52 resulted in power outages impacting 600,000 homes, over 6,000 cancelled flights, and 18
53 fatalities (Krekeler 2013; Picca et al. 2014; Ganetis and Colle 2015). Winter storms exhibit bands
54 with a variety of sizes, motions, and intensities, but most studies have investigated the primary
55 band, or a single snowband with length (L) > 200 km (e.g., Novak et al. 2004, Kenyon 2013,
56 etc.). In these previous studies, the use of radar data and mosaics based on Level III radar
57 reflectivities with 5 dB steps made it difficult to discern the groups of smaller, multiple bands
58 with $L < 200$ km that also enhance snowfall accumulation. For example, the 26–27 December
59 2010 East Coast winter storm produced over 10 finescale (5–20-km wide and 10–100-km long)
60 bands that led to over 6,000 cancelled flights and disrupted regional train service (Soltow 2011;
61 Kocin et al. 2011). A detailed analysis and comparison of the multi-band environment with that
62 of the single band within winter storms is needed to enhance understanding and prediction of
63 these bands.

64 Mesoscale bands found within the comma head of developing and mature extratropical
65 cyclones have been studied using conventional radar data for classification (e.g., Novak et al.
66 2004; 2010; Kenyon et al. 2013). The primary band, hereafter referred to as a single snowband
67 with $L > 200$ km, is typically found to the northwest of a surface low pressure center and
68 coincides with the ascending branch of the ageostrophic frontogenetical circulation. This ascent
69 and associated single band is narrowed and enhanced on the warm side of a mid-level frontal

70 boundary in an environment with conditional symmetric instability (CSI) or weak moist
71 symmetric stability (Emanuel 1985; Thorpe and Emanuel 1985; Xu 1989). Although single
72 snowbands are usually the focus of many winter mesoscale precipitation studies (e.g. Sanders
73 and Bosart 1985a,b; Wolfsberg et al. 1986; Novak et al. 2004, 2008, 2009, 2010, 2012; Moore et
74 al. 2005; Picca et al. 2014; Colle et al. 2014; Baxter and Schumacher 2017) smaller multi-bands,
75 defined as ≥ 2 parallel bands with $L < 200$ km, are often found embedded within the comma head
76 region of an extratropical cyclone and are less understood.

77 Although comparisons of case studies of banding within individual winter storms are
78 prevalent in the literature (e.g. Nicosia and Grumm 1999; Jurewicz and Evans 2004), multiyear
79 climatological studies consisting of > 5 storms are less numerous. Novak et al. (2004) used
80 mosaic radar reflectivity data to identify 88 cases from 1996 to 2001. Their study employed a
81 subjective classification scheme of the reflectivity data that included single bands, narrow cold-
82 frontal rainbands, and multi-bands. They compared the environments between single bands and
83 non-banded cases and found that bands occurred to the northwest of a cyclone associated with a
84 closed midlevel circulation with flow deformation and strong midlevel frontogenesis. The
85 climatological study by Novak et al. (2010) aimed to isolate the role of moist processes in the
86 evolution of the single-banded environment. Using the methodology from Novak et al. (2004),
87 they identified 144 heavy precipitation cases from 2002 to 2008, out of the 75 that exhibited a
88 closed 700-hPa low, 30 single-banded cases were examined. Novak et al. (2010) utilized single,
89 transitory and null categories in the classification scheme with no separation of multi-bands. The
90 main results of their study were that mid-level frontogenesis was stronger for banded events than
91 null events and conditional instability (CI) was more prevalent than CSI during single band
92 formation which challenged previous studies.

93 Most band classification studies have relied on the human eye for band identification and
94 classification (e.g., Novak et al. 2004; 2010; Kenyon et al. 2013). The first automated CONUS-
95 wide study of banded precipitation was created by Fairman et al. (2016). Using image processing
96 methods on composite radar imagery, they found that for Dec–Feb from 2003–2014 the
97 Northeast U.S. experiences relative peaks in the banded precipitation in the Tug Hill Plateau of
98 NY and lee of Lake Erie in western NY (likely associated with lake-effect precipitation bands)
99 and within the Ohio Valley extending across the Appalachians to the coast of NJ (likely
100 associated with banding within extratropical cyclones). This was a large-scale study focusing on
101 banded features with a major axis \geq 100 km, therefore smaller-scale bands, especially those
102 embedded within the comma head of extratropical cyclones, were not addressed.

103 Climatological studies of bands have been conducted for storms impacting the Midwest
104 and East Coast of the United States. A recent climatology of single-banded snowfall in Central
105 U.S. cyclones (between the Rocky and Appalachian Mountains) was conducted by Baxter and
106 Schumacher (2017) using 1-km composite radar imagery for 66 cyclones exhibiting \geq 4 in (10.16
107 cm) of accumulated snowfall during 5 cool seasons from 2006–2011. Their study manually
108 identified single bands that were \geq 250 km long and defined events every 3 hours within a storm.
109 Out of the 66 cyclones, there were 98 banded events and 38 non-banded events. The average
110 snowband lasted 5.2 h, was 45 km wide and 428 km long. Out of the banded events, 54 occurred
111 in the northeast (NE) quadrant relative to the cyclone center, 29 in the northwest (NW) quadrant,
112 and 15 within both northern quadrants. Out of the 38 non-banded events, the precipitation
113 coverage occurred in both northern quadrants for 28 events. Their study differed from that of the
114 East Coast winter storm analysis of Novak et al. (2004) in that this study found nearly twice as
115 many non-banded events and more single bands formed in the NE rather than the NW quadrant.

116 One goal of this research is to create a multi-year dataset consisting of cool season
117 (October through April) precipitation events that are identified and classified using
118 predominately objective methods. This is the first time a formal study has applied an automated
119 feature-based algorithm to determine snowband characteristics within a winter storm. This
120 dataset can be compared with that of previous climatological studies that relied on manual
121 classification methods. A potential caveat of using a solely an automated method is that various
122 fields, specifically radar reflectivity, can contain a wide range of values during one time in a
123 single storm. Subjective methods were also employed in this work in order to achieve consistent
124 classification among diverse storms.

125 Our paper aims to answer the following fundamental questions regarding single and
126 multi-bands in the comma head region of extratropical cyclones in the Northeast U.S.:

- 127 • What is the distribution of single bands, multi-bands, and non-banded events identified
128 using quasi-objective methods?
- 129 • How do vertical profiles of available moisture, instability, lift and wind shear differ
130 among multi-bands and single bands as well as non-banded precipitation areas in the
131 comma head?

132 This paper is organized as follows: Section 2 describes the methods used to identify and
133 classify precipitation bands in Northeast U.S. winter storms. Section 3 explores the cyclone-
134 relative band classification. Section 4 discusses the thermodynamic environment of the various
135 classifications of precipitation bands with a focus on contrasting known banding environmental
136 ingredients (i.e., moisture, instability, lift). Finally, section 5 summarizes the main results of this
137 banding study.

138

139 **2. Data and Methods**

140 *a. Case identification*

141 Cases were identified as cool season (October – April) low pressure systems that tracked
142 through the Northeast U.S. (NEUS) between 1996/97 – 2015/16 with ≥ 1.00 in (2.54 cm) of
143 liquid equivalent snowfall measured at ≥ 2 of 7 Automated Surface Observing System (ASOS)
144 stations across the NEUS (Fig. 1), which consisted of Portland, ME, Islip, NY, Boston, MA,
145 Philadelphia, PA, Bridgeport, CT, Providence, RI, and Newark, NJ (Hoban 2016). Over 150
146 cases were initially identified using this metric over 20 cool seasons, but 108 were ultimately
147 used based on radar data availability from six coastal radars (Fig. 1). Each case could span
148 multiple days, depending on the speed and extent of the affecting cyclone, but such days were
149 consolidated into a single case within the database.

150

151 *b. Cyclone tracking*

152 The band location relative to the surface cyclone center (i.e., nearest sea level pressure
153 minimum) is used in this study to provide a storm relative framework and to compare with recent
154 studies that highlight single bands that form in the northwest quadrant for NEUS storms (Novak
155 et al. 2004) or the northeast quadrant for continental U.S. storms (Baxter and Schumacher 2017).
156 The sea-level pressure data for the cyclone tracks were obtained from the from the 6-hourly 0.5°
157 NCEP Climate Forecast System Reanalysis (CFSR; Saha et. al. 2010) for years it was available
158 (1996–2010) and then from the 6-hourly 0.5° NCEP Climate Forecast System version 2 (CFSv2;
159 Saha et al. 2014) analyses (2011–2016). Other reanalysis data were considered including the
160 North American Regional Reanalysis (NARR). Charles and Colle (2009) showed that the NARR
161 had a weak sea level pressure bias for cyclones along the U.S. East Coast that was not shown
162 with the CFSR (Colle et al. 2013). Thus, the CFSR was used in favor of the NARR.

163 In order to track the extratropical cyclones on a common grid, the Hodges (1995) cyclone
164 tracking scheme was implemented according to the methodology provided in Colle et al. (2013).
165 Storms must track at least 1000 km and have a lifetime of \geq 24 h. The distance and lifetime
166 criteria are employed to remove features that are too short-lived or remain too stationary. If there
167 were multiple cyclones in the NEUS domain for a particular case, the cyclone subjectively
168 determined to be more associated with the observed precipitation as shown by the radar
169 reflectivity regional composite discussed in section 2c was manually selected. If a cyclone track
170 did not appear for a particular case because the cyclone was too weak to be identified then the
171 NOAA Weather Prediction Center (WPC) surface analyses for that date and time were used to
172 subjectively track the manually-identified low pressure center every 6-h. This supplemental
173 method was used for 2 storms. The cyclone tracks for each case used in this study are shown in
174 Figure 2.

175

176 *c. Regional composite radar dataset*

177 The radar data processing methods are described in detail in Hoban (2016) and Corbin
178 (2016) and are summarized in this section. Level II data from each of the six radars (KGYX,
179 KENX, KBOX, KOKX, KDIX, KDOX in Figure 1) were downloaded from the National Center
180 for Environmental Information (NCEI) radar archive and quality controlled to remove non-
181 meteorological echoes within individual elevation angles in polar coordinates. Analysis of
182 overlapping echo regions at equal distances between adjacent radars were used to apply a relative
183 radar reflectivity calibration with respect to KOKX observed values. KOKX was used because it
184 is close to the center of the study domain. The polar coordinate data were then interpolated to a 2
185 km x 2 km Cartesian grid at a constant elevation of 2 km AGL extending to a 200 km radius
186 from each site for every 6-10 min during each storm. For the duration of each storm, regional

maps of radar reflectivity were constructed by regridding each volume scan to a common 801 km x 801 km grid with 2 km horizontal grid spacing. Since the timing of volume scans among radars were not synchronized, KOKX was used as the central reference radar and data from other 5 radars were used as long as their volume start time was within 8 min of the volume start time at KOKX. There are sometimes gaps in the regional maps when data from an individual radar was not available in the NCEI archive. This analysis uses 5-minute Level II radar reflectivity data (0.5 dB precision) for every volume scan \pm 1 h from a 6-hourly analysis time during the storm. An important distinction between this study and previous studies such as Novak et al. (2004) and Kenyon (2013) is that they used Level III radar reflectivity data (5 dB precision).

196

197 *d. Objective identification of bands*

Precipitation bands are classified from automatically-detected objects from the gridded reflectivity data. The Method for Object-Based Diagnostic Evaluation (MODE) tool within the Model Evaluation Tools (MET) version 5.1 developed at the Developmental Testbed Center (DTC) at the Research Applications Laboratory (RAL) at the National Center for Atmospheric Research (NCAR) was used to objectively identify precipitation structures in the stitched regional composite radar data (Developmental Testbed Center 2015; Davis 2006a,b; Brown et al. 2007; Bullock et al. 2016).

Masking using an adaptive threshold was used to identify candidate objects with locally enhanced radar reflectivity which were then filtered based on geometric attributes to classify large bands, midsized bands, and undefined enhanced reflectivity regions. Masking was used to create a binary field that equals 1 above the threshold and 0 elsewhere. The adaptive threshold value for the reflectivity field varies during each case. Lawson and Gallus (2016) found that objective identification and verification of reflectivity data exhibited substantial sensitivity to the

211 reflectivity threshold chosen for summertime convection. They found that using too low of a
212 reflectivity value (5 dBZ) yielded too small of a sample size of objects, but using too high of a
213 value (40 dBZ) lost other features, i.e., stratiform precipitation. They concluded that the
214 threshold chosen should be done so to focus on the feature of interest. In a study of banding
215 throughout all four seasons, Fairman et al. (2016) chose a static threshold value of 20 dBZ.

216 In this study, the adaptive threshold for each case resulted from a series of tests on 10
217 example cases. Bulk statistics were computed from the regional composite reflectivity data for
218 both the entire storm duration and for individual 5-minute times during the storm. The following
219 quantities were calculated: minimum, lower-dectile, lower-octile, lower-quartile, median, mean,
220 upper-quartile, upper-octile, upper-dectile, and maximum. Data were used throughout the entire
221 regional radar composite domain and also tested on a sub-region centered over Long Island, NY.

222 The adaptive threshold that was found to work best for the 10 cases was the upper-sextile
223 of the reflectivity throughout the NEUS domain at *each* time within a storm. That meant that
224 17% of the reflectivity data is at or above this value, therefore highlighting the enhancements of
225 snowbands within the weaker, smaller reflectivity values. The upper-quartile was found to be too
226 low and failed to separate individual bands of higher reflectivity embedded within widespread
227 precipitation. The upper-octile was found to be too high of a threshold that trimmed bands down,
228 therefore underestimating their spatial characteristics. The upper-sextile threshold calculated at
229 each time step performed best at separating out individual multi-bands from non-banded
230 precipitation and any nearby large bands and was used to create the masked field.

231 Once the masked field is computed, objects are identified with the MODE tool as regions
232 that are continuous in space. If there is even one grid point separating the objects, they are
233 identified as separate objects. Attributes are computed for each object and include the object area

234 which is the number of grid squares an object occupies and the centroid, or geometric center, of
235 an object. The length, width, aspect ratio, and axis angle are computed by fitting a rectangle
236 around each object. The aspect ratio is the ratio of the short axis to the long axis. The axis angle
237 is the angle of the long axis of the rectangle relative to 90° (east).

238 There is a large variation of storm (and reflectivity) intensity among all 108 storms that
239 ultimately motivated the time-varying adaptive threshold. However, this time-varying threshold
240 was not without its limitations. There were times when a weaker band existed during a stronger
241 storm with too high a reflectivity threshold that resulted in a failure of the method. The threshold
242 was skewed higher by offshore rain in several storms when a portion of the storm was over warm
243 Gulf Stream waters. Ultimately, the objective method did not work well for 8 out of 108 storms
244 during which manual methods had to be employed to subjectively identify (i.e., use the human
245 eye on the raw observed reflectivity field) instead of relying on the objective methods for 5 cases
246 of both a single band with multi-bands and 3 cases of multi-bands only.

247

248 *e. Classification of bands*

249 Classification was first completed by post-processing the data output from MODE.
250 Objects were determined to be snowbands if their aspect ratios (length of minor axis divided by
251 the length of major axis) was ≤ 0.5 . The bands were additionally classified into large bands, mid-
252 sized bands, or undefined according to the length and width criteria provided in Table 1.

253 Next, both the classified field and the raw reflectivity field were analyzed to subjectively
254 classify dominant banding types at each 6-hourly analysis time during a case (i.e., 0000, 0600,
255 1200, 1800 UTC). The classifications were one of four different categories based on the types of
256 objects that were identified ± 1 h of the analysis time within one boxed sounding domain

extending 150 km from each of the 6 sounding locations in Figure 1 (i.e., KGYX, KALB, KCHH, KOKX, KIAD, KWAL) every 6 h during a case. An event was classified if the radar echo was found in $\geq 50\%$ of the sounding domain box for ≥ 2 h. The use of 6-hourly events is consistent with what had been done in previous studies (e.g., Novak et al. 2004; Baxter and Schumacher 2017). The four storm-band categories (Table 2) were adapted from Novak et al. (2004, their Table 1). The first category is for a storm that exhibits a large band ($L \geq 200$ km) and no other identified structures in the sounding domain and is termed the single band category (SINGLE, sample size =5). The second category is for a storm that exhibits ≥ 2 mid-sized bands that are parallel to each other and move similarly in the sounding domain and is the multi-band category (MULTI, sample size =35). The third category is for a storm that exhibits a large band accompanied by mid-sized bands and is termed the both single band and multi-bands category (BOTH, sample size =107). In the analysis below, we examine separately the environment of the large band (BOTH-Large) and concurrent multi-bands (BOTH-Mid-sized bands). The fourth and final category is for storms that exhibit none of the previous linear precipitation structure classification criteria and is termed the non-banded category (NONE, sample size = 46). Figure 3 shows examples of cases in each of the four categories.

273

274 *f. Subjective classification of banding events for cyclone stage and movement*

275 Storms were additionally sub-classified based on both cyclone stage and band motion.
276 Cyclone maturity has been used in refining climatological studies such as by Novak et al. (2010)
277 who used the presence of a closed 700-hPa circulation to differentiate comma head cases (i.e.,
278 stronger cyclones that would likely have precipitation wrapping around the center to form a
279 comma head) from non-comma head cases within their 6-year study. Kenyon et al. (2013) looked

280 into band motion with a special focus on both laterally translating and radially pivoting single
281 bands.

282 Cyclone maturity during each 6-hour time was classified as either developing or mature
283 determined manually using the WPC surface analyses following the Norwegian and Shapiro and
284 Keyser cyclone models (Bjerknes and Solberg 1922; Shapiro and Keyser 1990; Colle et al.
285 2014). Specifically, developing storms were defined as having an open wave frontal structure
286 while mature cyclones were at the start of the occluded stage defined as when circulations
287 around a cyclone create an occluded front that separates the cold air behind the cold front from
288 the warm air ahead of the cold front (Schultz and Vaughan 2010). The location of the
289 precipitation band relative to the cyclone center can depend on cyclone maturity, such as forming
290 north of a warm front in a developing cyclone versus northwest along the occluded front in a
291 mature cyclone (Schultz and Vaughan 2010). The four storm-band categories were further
292 classified into developing and mature cyclones resulting in eight categories.

293 The 5-minute interval animations of reflectivity and classified bands were used to classify
294 geographic-centric band motion by animating ± 1 h on either side of the 6-hourly analysis time.
295 Band motion with respect to the long axis of the band was assessed. One or more bands were
296 classified as moving perpendicular or parallel to their long axis or axes. The perpendicular
297 classification is comparable to the laterally translating and pivoting classifications used by
298 Kenyon et al. (2013). The parallel classification is comparable to the laterally quasi-stationary
299 classification used by Kenyon et al. (2013). The results from their study showed that various
300 band motions resulted from different synoptic and mesoscale environments, so therefore were
301 taken into account within this study for comparison. The eight classifications of band type and
302 cyclone strength were further sub-classified into perpendicular and parallel moving bands,

303 resulting in 12 different classification categories. The non-banded (NONE) classification was
304 classified into developing or mature cyclones, but no motion criteria were applied because there
305 were no defined bands to base the classification on.

306

307 *g. Analysis of band environment*

308 Observed soundings from the six upper-air locations over the Northeast U.S. are available
309 approximately every 12 h (Fig. 1). To increase the temporal frequency of available vertical
310 profiles to every 6-h, vertical profiles were also derived from the 0.5° resolution CFSR. This is
311 the same analysis data used by Kenyon et al. (2013) for their environmental band analysis. The
312 Climate Forecast System version 2 (CFSv2; Saha et al. 2014), which was used for dates later
313 than 2010, have data approximately every 38 km horizontally with 64 vertical pressure levels
314 (Saha et al. 2014). Our analysis focus is above the boundary layer, thus minimizing the effect of
315 terrain or surface type differences.

316 The accuracy of these CFSR grid point profiles was determined by comparing 1292
317 available soundings every 6 h during each of the 108 events from the 6 coastal sites (Fig. 1).
318 Above the boundary layer (> 2 km AGL), the mean error of temperature was typically $\pm 2^{\circ}\text{C}$ and
319 relative humidity $\pm 15\%$. The mean errors for mixing ratio above the boundary layer are typically
320 within $\pm 1 \text{ g kg}^{-1}$ and are within $\pm 2 \text{ K}$ for potential temperature. Based on this evaluation, the
321 CFSR-derived soundings were considered a reasonable estimate to the observed atmosphere for
322 the purposes of our analysis.

323 Each 6-h event corresponds to bands (or lack thereof) within one specific domain that is
324 centered on and extends ~ 150 km from a sounding site (Fig. 1). Vertical profiles based on 6-h
325 CSFR reanalysis were taken at the nearest grid point to MODE-identified band centroid (see
326 sections 1d–e) within a sounding domain. For times during which multi-bands were identified,

327 profiles were taken from each individual mid-sized band. For times during which both large
328 bands and mid-sized bands were observed, profiles were taken from the large band (BOTH-
329 Large band) and any available mid-sized band (BOTH-Mid-sized band) separately. For non-
330 banded events, the center of the sounding domain was used for the profile extraction.

331

332 **3. Cyclone-relative Band Classification**

333 *a. Distribution by event*

334 The results of the approximately 6-hourly event classifications produced a total of 193
335 events from the 108 cases. The distribution of the sounding domain of each classification relative
336 to the cyclone center is provided in Figure 4. The initial classification into the four standard
337 categories is as follows: 5 SINGLE, 35 MULTI, 107 BOTH, and 46 NONE. All 5 SINGLE
338 events were associated with a mature cyclone and most occurred in the northwest quadrant of a
339 cyclone (Fig. 4a). MULTI events were approximately equitably distributed between developing
340 (18) and mature (17) cyclones. BOTH events were less often observed with developing (43) than
341 mature cyclones (64). NONE events were more often associated with developing (29) than
342 mature cyclones (17). The results of the final application of the geographic-centric band
343 movement classification are provided in Table 2. While the distribution of counts of MULTI
344 events was similar for both developing and mature cyclones, the bands favored parallel
345 movement when associated with developing cyclones versus a perpendicular movement when
346 associated with mature cyclones. For both mature and developing cyclones, more multi-bands
347 occurred in the northeast quadrant than the northwest quadrant (Fig. 4b). A similar relationship
348 for band motion is evident when comparing the motion associated with BOTH events. Parallel
349 band motion is predominant during developing cyclones versus perpendicular motion during
350 mature cyclones. Perpendicular band motion classified events typically occurred in the northwest

351 quadrant of a mature cyclone, while parallel band motion classified events typically occurred in
352 the northeast quadrant of a developing cyclone (Fig. 4c). Non-banded events were predominantly
353 in the eastern quadrants, favoring the northeast quadrant (Fig. 4d).

354 Figure 5 shows the band orientation in addition to the location relative to the cyclone
355 center for large bands from SINGLE and BOTH events for developing and mature cyclones.
356 There is a cluster in the northwest quadrant of bands oriented southwest-northeast which is
357 observed to match the orientation of enhanced baroclinic zones that will be analyzed in section 4.
358 More large bands ≥ 500 km from the cyclone center in the northeast quadrant are associated with
359 developing cyclones (7) rather than mature cyclones (2). The more west-east orientation of these
360 large bands is thought to be due to their collocation with the warm front. The band orientations
361 and clustering in the northern quadrants is consistent with similar analysis conducted by Novak
362 et al. (2004) and Baxter and Schumacher (2017).

363

364 **4. Vertical Profile Analysis**

365 Comparisons of the thermal, moisture, and kinematic variables from a representative
366 profile from 1000 hPa to 300 hPa from each event were examined. Significance is assessed via
367 bootstrapping (Wilks 2011); each classification dataset is resampled by replacing randomly
368 1,000 times. For all four datasets, the size for each resample is equivalent to the total number of
369 events in the original dataset (5 SINGLE, 35 MULTI, 107 BOTH-Large band subset, 107
370 BOTH-Mid-sized band subset, 46 NONE).

371 Given the common location within the comma head of a cyclone, there is little variation
372 in temperature profiles among the four classifications (Figs. 6a–f). There was some variability in
373 the presence of an unsaturated layer which is the most pronounced in the SINGLE classification
374 (Figs. 6f–j). Individual profiles of saturation equivalent potential temperature (θ_e^*) show the

375 presence of weak conditional stability indicated by a small increase in θ_e^* with height for all
 376 classifications (Figs. 7a–e). Over 20% of SINGLE and BOTH-Large bands profiles exhibited a
 377 50-hPa deep conditionally unstable layer ($\leq -0.02 \text{ K hPa}^{-1}$) compared to < 5% of MULTI and
 378 BOTH-Mid-sized bands (not shown). The MULTI and BOTH-Mid-sized band events have larger
 379 average wind shear (950–750 hPa) values, $\sim 5.8 \text{ m s}^{-1}$ and 5.67 m s^{-1} , respectively, compared to
 380 the $\sim 3.7 \text{ m s}^{-1}$ and $\sim 3.0 \text{ m s}^{-1}$ for SINGLE and BOTH-Large bands, respectively (Fig. 7j; Table
 381 3).

382 Average profiles of 2-D Petterssen (1936) frontogenesis (Eq. 1; as in Novak et al. 2004,
 383 their Eq. 1) were computed for SINGLE and BOTH-Large band subset (Figs. 8a,c) and
 384 compared to BOTH-Mid-sized band subset and MULTI (Figs. 8b,d). Larger, single bands are
 385 associated with stronger forcing for lift via frontogenesis than multi-bands, likely related to their
 386 preferential location in the northwest quadrant of low pressure systems (Table 3).

$$387 F_{2D} = \frac{1}{|\nabla\theta|} \left(-\frac{\partial\theta}{\partial x} \left(\frac{\partial u}{\partial x} \frac{\partial\theta}{\partial x} + \frac{\partial v}{\partial x} \frac{\partial\theta}{\partial y} \right) - \frac{\partial\theta}{\partial y} \left(\frac{\partial u}{\partial y} \frac{\partial\theta}{\partial x} + \frac{\partial v}{\partial y} \frac{\partial\theta}{\partial y} \right) \right) \quad \text{Eq. 1}$$

388 Equation 1 of frontogenesis (F_{2D}) includes the gradients in the zonal (x) and meridional (y)
 389 directions of potential temperature (θ), and the zonal and meridional components of the wind (u
 390 and v , respectively). Non-banded and multi-banded environments were associated with lower
 391 values of frontogenesis than other classifications (Fig. 8).

392 Conditional symmetric instability (CSI) is indicated by negative values of saturation
 393 equivalent potential vorticity (MPV*; Eqs. 2-3; McCann 1995) in the absence of inertial and
 394 conditional instability (Schultz and Schumacher 1999).

$$395 MPV^* = \frac{1}{\rho} \eta \cdot \nabla \theta_e^* \quad \text{Eq. 2}$$

$$396 MPV^* = g \left(\left(\frac{\partial \theta_e^*}{\partial x} \frac{\partial v}{\partial P} \right) - \left(\frac{\partial \theta_e^*}{\partial y} \frac{\partial u}{\partial P} \right) - \frac{\partial \theta_e^*}{\partial P} \left(\frac{\partial v}{\partial x} - \frac{\partial u}{\partial y} + f \right) \right) \quad \text{Eq. 3}$$

397 in which g is gravity, P is pressure, f is the Coriolis parameter equal to $2Q\sin\phi$ where ϕ is
398 latitude, ρ is the density, η is the absolute vorticity vector and θ_e^* is the saturation equivalent
399 potential temperature. Equation 3 follows from Equation 2 assuming the horizontal gradient of
400 the vertical wind speed is small and can be neglected. Banded precipitation has been related to
401 CSI (negative MPV*) via the following components of the conceptual model put forth by Clark
402 et al. (2002): (1) a region of mid-troposphere frontogenesis over the banded precipitation region,
403 (2) a saturated mesoscale updraft on the warm side of the frontogenesis region, (3) negative
404 MPV production near the updraft dominated by differential vertical θ_e transport, and (4) release
405 of CSI leading to banded precipitation. Negative value of MPV* would indicate the presence of
406 CSI in the absence of CI, a known instability responsible for enhancing circulations associated
407 with some single bands (Novak et al. 2010). Average profiles of MPV* were calculated from the
408 4 closest grid points centered on the band location for all vertical levels. CSI is evident in the
409 average profiles of all classification types below 600 hPa (Figs. 8f–i). The most negative values
410 in the average profiles of MPV* are found between 900-800-hPa for all classifications, with
411 $\text{MPV}^* < 0$ and statistically insignificant differences among the classifications between 700-550-
412 hPa (Fig. 8j).

413 Looking at one particular level (e.g., 700 hPa), frontogenesis was calculated along with
414 the 750-650-hPa layer-averaged value of MPV* (Fig. 9). The NONE, MULTI, and BOTH-Mid-
415 sized events exhibit the weakest frontogenesis ($< 2 \text{ K (100 km 1 h)}^{-1}$). BOTH-Large band events
416 had the largest frontogenetical values with 12 of 107 (~11%) events associated with
417 frontogenesis $> 1.5 \text{ K (100 km 1 h)}^{-1}$. The MULTI environment showed relatively weak
418 frontogenesis values with 34 events $< 1.5 \text{ K (100 km 1 h)}^{-1}$. Two BOTH-Mid-sized events
419 exhibited 700–600-hPa conditionally unstable layers (θ_e^* decreasing with height) but 99 of 107

420 (93%) events were associated with moist symmetric instability ($\text{MPV}^* < 0$). None of the MULTI
421 events exhibited conditional instability but 34 events exhibited conditional symmetric instability.
422 SINGLE and BOTH-Large Subset classifications exhibited more layers of CI than NONE,
423 MULTI, and BOTH-Mid-sized subset (not shown).

424 A simple frontogenesis threshold does not distinguish among band categories as shown in
425 Figure 10. While SINGLE and BOTH-Large bands occurred in environments of strong
426 frontogenesis, they also occurred with moderate and with weak frontogenesis. MULTI, BOTH-
427 Mid-sized bands and NONE occurred in conditions of moderate to weak frontogenesis. The
428 combination of MPV and frontogenesis does not clearly distinguish among band categories
429 either. Hence, while the presence of strong frontogenesis increases the likelihood of a single
430 band forming, these long bands as well as shorter multi-bands do form in weaker forcing
431 conditions.

432

433 **5. Summary and Discussion**

434 A combination of objective and subjective approaches for the classification of bands of
435 108 NEUS winter storms from 1996–2016 was conducted. This is the first formal attempt to
436 automatically identify bands within winter storms using a feature-based algorithm. The dataset
437 was comprised of extratropical cyclones that produced $\geq 1.00 \text{ in}$ (2.54 cm) per day liquid
438 equivalent snowfall at least 2 of 7 ASOS stations along the eastern seaboard from Delaware to
439 Maine. Regional composite 2-km AGL radar reflectivity data from six coastal NEUS radars were
440 used to identify and classify bands using the Model Evaluation Tools (MET) Method for Object-
441 based Diagnostic Evaluation (MODE), specifically into large bands ($L \geq 200 \text{ km}$) and mid-sized
442 bands ($L < 200 \text{ km}$) both with aspect ratios (ratio of width to length) ≤ 0.5 . At each 6-hourly

443 analysis time, the portions of the storm falling within each of six 300 km x 300 km boxes
444 centered on operational sounding sites were categorized as containing either: a single band only
445 (SINGLE), multi-bands only (MULTI), both single and multi-bands (BOTH), or as non-banded
446 (NONE) for radar echoes present in $\geq 50\%$ of the box ≥ 2 h. This resulted in 193 classified storm
447 sub-periods from 108 storms with the most common categories being BOTH (107) and NONE
448 (46), followed by MULTI (35) and SINGLE (5) (Table 2). This study found that single bands
449 unaccompanied by multi-bands are actually quite rare compared to the findings of previous
450 studies. This discrepancy is likely a result of the 5-dBZ binning of the reflectivity field that
451 others used, compared to our analysis that used 0.5 dB precision Level 2 radar data and a method
452 that detected locally enhanced features relative to a changing background.

453 Additional information was used to further sub-classify the categories by their association
454 with a developing or mature cyclone and the type of geographic-centric band movement
455 exhibited as being either moving perpendicular to the long axis or moving parallel to the long
456 axis. Developing cyclones were predominantly associated with parallel moving bands (69%) that
457 were clustered in the northeast quadrant. Mature cyclones most often exhibited BOTH (48%) in
458 the northwest quadrant, MULTI (17%) in the northeast quadrant, NONE (17%) in the eastern
459 quadrants, and SINGLE (5%) in the northwest quadrant. Mature cyclones were predominantly
460 associated with perpendicular moving bands (87%) that occurred most frequently in the
461 northwest quadrant of the cyclone.

462 CFSR and CFSv2 analyses were used to compare environmental variables of the known
463 important single banding ingredients of lift, instability, and moisture for the different banding
464 classifications. Strong frontogenesis increases the likelihood of a single band forming, but these
465 long bands as well as shorter multi-bands can form in an environment of weak frontogenesis.

466 This suggests that given an environment of weak frontogenesis, other lifting processes may need
467 to be explored, such as gravity waves or vertical shear instabilities. MULTI and BOTH-Large
468 profiles exhibited larger 1000–700-hPa wind shear compared to SINGLE and BOTH-Large and
469 the importance of this result will be explored in a future case study.

470 MULTI and BOTH-Mid-sized bands typically exhibit a 200-hPa layer of conditional
471 symmetric instability (CSI indicated by $\text{MPV}^* < 0 \text{ PVU}$) more often than conditional instability
472 (CI). Previous studies suggest that CSI is the dominant instability responsible for multiple bands
473 from analysis of one case or synoptic situation (e.g., Shields et al. 1991, Xu 1992) to three cases
474 (Nicosia and Grumm 1999). Furthermore, precipitation bands are not always associated with CSI
475 (Schultz and Schumacher 1999). Novak et al. (2010) found that CI occurred more often than CSI
476 near the time of band formation for dozens of single band cases within mature cyclones. In this
477 study, we analyze all times when bands are present which includes: formation, development,
478 maturation, and dissipation. CSI was evident in the average profiles of all classification types
479 below 600 hPa (Figs. 8f–i), but CI was more associated with SINGLE and BOTH-Large bands
480 rather than MULTI and BOTH-Mid-sized bands. In particular, CSI was more common than CI
481 between 900–800-hPa among all five classifications. NONE events show shallow near-surface
482 layers of CSI, but it might not be released without lifting via frontogenesis. There was no
483 significant difference in the third banding ingredient, moisture, among the classifications likely
484 due to the common location in the near-saturated environment of the cyclone comma head.
485 General differences among banded environments are provided in this paper. Future work could
486 utilize both observations and a high-resolution mesoscale model to explore some of the
487 mechanisms for multi-band development as well as analyze the evolutions of single and multi-
488 bands, separately, to examine differences in more detail.

489

490 **Acknowledgements**

491 This work was supported by the National Science Foundation (AGS-1347491 and AGS-
492 1347499). Special thanks to Luke Allen, Sara Berry, Michael Tai Bryant, Nicole Corbin, Jason
493 Endries, Levi Lovell, Matthew Miller, Emma Scott, Laura Tomkins for their work with radar
494 data processing and analysis.

495

496

497 **References**

498 Baxter, M. and P. Schumacher, 2017: Distribution of single-banded snowfall in Central United
499 States cyclones. *Wea. Forecasting*, **32**, 533–554.

500 Bjerknes, J., and H. Solberg, 1922: Life cycle of cyclones and the polar front theory of
501 atmospheric circulation. *Geofys. Publ.*, **3**, 3–18.

502 Brown, B.G., R. Bullock, J. Halley Gotway, D. Ahijevych, C. Davis, E. Gilleland, and L.
503 Holland, 2007: Application of the MODE object-based verification tool for the evaluation
504 of model precipitation fields. *AMS 22nd Conference on Weather Analysis and*
505 *Forecasting and 18th Conference on Numerical Weather Prediction*, 25–29 June, Park
506 City, Utah, Amer. Meteor. Soc.

507 Bullock, R. G., B. G. Brown, and T. L. Fowler, 2016: Method for object-based diagnostic
508 evaluation. NCAR Tech. Note. NCAR/TN-532+STR, 84 pp, doi:10.5065/D61V5CBS.

509 Charles, M. E., and B. A. Colle, 2009: Verification of extratropical cyclones within the NCEP
510 operational models. Part I: analysis errors and short-term NAM and GFS forecasts. *Wea.*
511 *Forecasting*, **24**, 1173–1190.

512 Clark, J. H. E., R. P. James, and R. H. Grumm, 2002: A reexamination of the mechanisms
513 responsible for banded precipitation. *Mon. Wea. Rev.*, **130**, 3074–3086.

514 Colle, B. A., D. Stark, and S. E. Yuter, 2014: Surface microphysical observations within East

- 515 Coast winter storms on Long Island, NY. *Mon. Wea. Rev.*, **142**, 3126–3146.
- 516 Colle, B. A., Z. Zhang, K. A. Lombardo, E. Chang, P. Liu, and M. Zhang, 2013: Historical
517 evaluation and future prediction of Eastern North American and Western Atlantic
518 extratropical cyclones in the CMIP5 models during the cool season. *J. Climate*, **26**, 6882–
519 6903.
- 520 Corbin, N. A., 2016: Northern California’s Central Valley spatial precipitation patterns
521 associated with atmospheric rivers under different environmental conditions, M.S.
522 Thesis, Dept. of Marine, Earth, Atmospheric Sciences, North Carolina State University,
523 227 pp.
- 524 Davis, C.A., B.G. Brown, and R.G. Bullock, 2006a: Object-based verification of precipitation
525 forecasts, Part I: Methodology and application to mesoscale rain areas. *Mon. Wea. Rev.*,
526 **134**, 1772–1784.
- 527 Davis, C.A., B.G. Brown, and R.G. Bullock, 2006b: Object-based verification of precipitation
528 forecasts, Part II: Application to convective rain systems. *Mon. Wea. Rev.*, **134**, 1785–
529 1795.
- 530 Developmental Testbed Center, 2015: MET: Version 5.1 Model Evaluation Tools Users Guide.
531 317 pp. [Available online at <http://www.dtcenter.org/met/users/docs/overview.php>.]
- 532 Emanuel, K. A., 1985: Frontal circulations in the presence of small moist symmetric stability.
533 *J. Atmos. Sci.*, **42**, 1062–1071.
- 534 Fairman Jr, J. G., D. M. Schultz, D. J. Kirshbaum, S. L. Gray, and A. I. Barrett, 2016:
535 Climatology of banded precipitation over the contiguous united states. *Mon. Wea. Rev.*,
536 **144**, 4553–4568.
- 537 Ganetis, S., and B. Colle, 2015: The thermodynamic and microphysical evolution of an intense

- 538 snowband during the Northeast U.S. blizzard of 8-9 February 2013. *Mon Wea. Rev.*, **143**,
539 4104-4125.
- 540 Hoban, N. P., 2016: Observed characteristics of mesoscale banding in Coastal Northeast U.S.
541 snow storms, M.S. Thesis, Dept. of Marine, Earth, Atmospheric Sciences, North Carolina
542 State University, 66 pp.
- 543 Hodges, K. I., 1995: Feature tracking on the unit sphere. *Mon. Wea. Rev.*, **123**, 3458–3465.
- 544 Jurewicz, M. L., and M. S. Evans, 2004: A Comparison of two banded, heavy snowstorms
545 with very different synoptic settings. *Wea. Forecasting*, **19**, 1011–1028.
- 546 Kenyon, J. S., 2013: The motion of mesoscale snowbands in Northeast U.S. winter storms, M.S.
547 Thesis, Dept. of Atmos. and Environmental Sci., University at Albany, State University
548 of New York, 108 pp.
- 549 Kocin, P., L. W. Uccellini, J. Alpert, B. Ballish, D. Bright, R. Grumm, and G. Manikin, 2011:
550 The blizzard of 25-27 December 2010: Forecast assessment. NOAA/NCEP event review.
551 [Available online at http://www.wpc.ncep.noaa.gov/winter_storm_summaries/
552 event_reviews/2010/December25_27_2010_Blizzard.pdf.]
- 553 Krekeler, J., 2013: Great Lakes to Northeast major winter storm. NOAA/NCEP/WPC event
554 review. [Available online at http://www.wpc.ncep.noaa.gov/winter_storm_summaries/
555 event_reviews/2013/Great_Lakes_Northeast_Winter_Storm_Feb2013.pdf.]
- 556 Lawson, J. R., and W. A. Gallus, 2016: Adapting the SAL method to evaluate reflectivity
557 forecasts of summer precipitation in the central United States. *Atmos. Sci. Lett.*, **17**, 524-
558 530.
- 559 McCann, D. W., 1995: Three-dimensional computations of equivalent potential vorticity. *Wea.*
560 *Forecasting*, **10**, 798–802.

- 561 Moore, J. T., C. E. Graves, S. Ng, and J. L. Smith, 2005: A process-oriented methodology
562 toward understanding the organization of an extensive mesoscale snowband: A diagnostic
563 case study of 4–5 December 1999. *Wea. Forecasting*, **20**, 35–50.
- 564 Nicosia, D. J., and R. H. Grumm, 1999: Mesoscale band formation in three major Northeastern
565 United States snowstorms. *Wea. Forecasting*, **14**, 346–368.
- 566 Novak, D. R., L. F. Bosart, D. Keyser, and J. S. Waldstreicher, 2004: An observational study of
567 cold season–banded precipitation in Northeast U.S. cyclones. *Wea. Forecasting*, **19**, 993–
568 1010.
- 569 Novak, D. R., and B. A. Colle, 2012: Diagnosing snowband predictability using a multimodel
570 ensemble system. *Wea. Forecasting*, **27**, 565–585.
- 571 Novak, D. R., B. A. Colle, and A. R. Aiyyer, 2010: Evolution of mesoscale precipitation band
572 environments within the comma head of Northeast U.S. cyclones. *Mon. Wea. Rev.*, **138**,
573 2354–2374.
- 574 Novak, D. R., B. A. Colle, and R. McTaggart-Cowan, 2009: The role of moist processes in the
575 formation and evolution of mesoscale snowbands within the comma head of Northeast
576 U.S. cyclones. *Mon. Wea. Rev.*, **137**, 2662–2686.
- 577 Novak, D. R., B. A. Colle, and S. E. Yuter, 2008: High-resolution observations and model
578 simulations of the life cycle of an intense mesoscale snowband over the Northeastern
579 United States. *Mon. Wea. Rev.*, **136**, 1433–1456.
- 580 Petterssen, S., 1936: Contribution to the theory of frontogenesis. *Geofys. Publ.*, **11**(6), 1–27.
- 581 Picca, J. C., D. M. Schultz, B. A. Colle, S. Ganetis, D. R. Novak, and M. Sienkiewicz, 2014: The
582 value of dual-polarization radar in diagnosing the complex microphysical evolution of an
583 intense snowband. *Bull. Amer. Meteor. Soc.*, **95**, 1825–1834.

- 584 Saha, S., and Coauthors, 2010: The NCEP climate forecast system reanalysis. *Bull. Amer.*
585 *Meteor. Soc.*, **91**, 1015–1057.
- 586 Saha, S., and Coauthors, 2014: The NCEP climate forecast system version 2. *J. Climate*, **27**,
587 2185–2208.
- 588 Sanders, F., and L. F. Bosart, 1985a: Mesoscale structure in the Megalopolitan snowstorm of 11–
589 12 February 1983. Part I: frontogenetical forcing and symmetric instability. *J. Atmos.*
590 *Sci.*, **42**, 1050–1061.
- 591 Sanders, F., and L. F. Bosart, 1985b: Mesoscale structure in the Megalopolitan snowstorm, 11–
592 12 February 1983. Part II: doppler radar study of the New England snowband. *J. Atmos.*
593 *Sci.*, **42**, 1398–1407.
- 594 Schultz, D. M., and P. N. Schumacher, 1999: The use and misuse of conditional symmetric
595 instability. *Mon. Wea. Rev.*, **127**, 2709–2732.
- 596 Schultz, D. M., and G. Vaughan, 2010: Occluded fronts and the occlusion process: A fresh
597 look at conventional wisdom. *Bull. Amer. Meteor. Soc.*, **92**, 443–466.
- 598 Shapiro, M. A., and D. Keyser, 1990: Fronts, jet streams and the tropopause. Extratropical
599 cyclones: The Erik Palmén memorial volume, C.W.Newton and E. O. Holopainen, Eds.,
600 *Amer. Meteor. Soc.*, pp. 167–191.
- 601 Shields, M. T., R. M. Rauber, and M. K. Ramamurthy, 1991: Dynamical forcing and mesoscale
602 organization of precipitation bands in a Midwest winter cyclonic storm. *Mon. Wea. Rev.*,
603 **119**, 936–964.
- 604 Soltow, M., 2011: December 25-27, 2010, Winter storm, Eastern United States.
605 NOAA/NCEP/WPC event review. [Available online at <http://www.wpc.ncep.noaa.gov/>

606 winter_storm_summaries/event_reviews/2010/Eastern_US_WinterStorm_December_201
607 .pdf.]

608 Thorpe, A. J., and K. A. Emanuel, 1985: Frontogenesis in the presence of small stability to
609 slantwise convection. *J. Atmos. Sci.*, **42**, 1809–1824.

610 Wilks, D.S., 2011: *Statistical methods in the atmospheric sciences*, 3rd Ed. International
611 Geophysics Series, Vol. 100, Academic Press, 704 pp.

612 Wolfsberg, D. G., K. A. Emanuel, and R. E. Passarelli, 1986: Band formation in a New England
613 winter storm. *Mon. Wea. Rev.*, **114**, 1552–1569.

614 Xu, Q., 1989: Extended Sawyer–Eliassen equation for frontal circulations in the presence of
615 small viscous moist symmetric stability. *J. Atmos. Sci.*, **46**, 2671–2683.

616 Xu, Q., 1992: Formation and evolution of frontal rainbands and geostrophic potential vorticity
617 anomalies. *J. Atmos. Sci.*, **49**, 629–648.

618

619 **Table and Figure Captions**

620 **Table 1.** Criteria used to objectively classify objects output from the MET MODE tool applied to
621 stitched regional composite reflectivity data.

622 **Table 2.** Case classification by band type, cyclone stage, and band motion for 6-hourly events
623 during banded cases.

624 **Table 3.** Environmental banding ingredients for each classification type.

625 **Figure 1.** Map showing locations of six upper-air sites (green circles) used for vertical profiles
626 through regional classification given by each box bounding ~150-km around the upper-
627 air site. Locations of regional NWS WSR-88D radar (red circles) and Automated Surface
628 Observing System (ASOS) sites (purple squares) are shown.

629 **Figure 2.** Sea level pressure (SLP) along each of the 108 cyclone tracks in the study with points

630 along the track colored by SLP with warmer colors indicating weaker cyclones and
631 cooler colors indicating stronger cyclones.

632 **Figure 3.** Examples of 2-km AGL stitched regional composite reflectivity and the resulting
633 classified objects from the MET MODE tool output for the four banding classifications
634 exhibited in Northeast U.S. winter storms, (a) a large, single band, (b) multi-bands, (c)
635 both single and multi-bands, and (d) non-banded.

636 **Figure 4.** Distance and angle from cyclone low pressure center for 193 events for (a) SINGLE
637 events for mature (filled circle) and developing (open circle) cyclones for parallel moving
638 bands (light green) and perpendicular moving bands (dark green), (b) MULTI events for
639 mature (asterisk) and developing (plus sign) cyclones for parallel moving bands (light
640 blue) and perpendicular moving bands (dark blue), (c) BOTH events for mature (asterisk)
641 and developing (cross) cyclones for parallel moving bands (light purple) and
642 perpendicular moving bands (dark purple), (d) NONE events for mature (filled diamond)
643 and developing (open diamond) cyclones. The radial distance is in kilometers and the
644 angle from the cyclone to the sounding location at the center of the domain of the
645 classified event is in degrees.

646 **Figure 5.** Large band locations and orientations relative to the cyclone center (origin of plot)
647 with the radius in km and angle in degrees. Bands associated with mature cyclones are in
648 blue and developing cyclones are in red.

649 **Figure 6.** Vertical profiles of (a–e) temperature ($^{\circ}\text{C}$) and (f–j) relative humidity (%) for events
650 classified as (a,f) SINGLE, (b,g) MULTI, (c,h) BOTH-Large bands subset, (d,i) BOTH-
651 Mid-sized bands subset, (e,j) NONE events. Bold lines denote the mean profile for each

652 classification with markers indicating 2.5th and 97.5th percentiles of the mean with 95%
653 confidence.

654 **Figure 7.** As in Figure 6 but for (a–e) saturation equivalent potential temperature (K) and (f–j)
655 wind speed (kts). Red profiles in (a–d) indicate those that exhibit a conditionally unstable
656 50-hPa layer ($d\theta_e^*/dP \leq 0.02 \text{ K hPa}^{-1}$).

657 **Figure 8.** As in Figure 6 but for (a–e) frontogenesis (K 100 km⁻¹ h⁻¹) and (f–j) saturation
658 equivalent potential vorticity (MPV*, PVU).

659 **Figure 9.** The relationship between 750–650-hPa averaged saturation equivalent potential
660 vorticity (MPV*, PVU) on the abscissa and 700-hPa frontogenesis (K 100 km⁻¹ h⁻¹) on
661 the ordinate for (a) SINGLE, (b) MULTI, (c) BOTH-Large bands subset, (d) BOTH-Mid-
662 sized bands subset, and (e) NONE classified events from developing (DEV) or mature
663 (MAT) cyclones exhibiting perpendicular (PERP) or parallel (PARA) band motion.

664 **Figure 10.** Distribution of 800–700-hPa average frontogenesis for all events in the dataset
665 colored by classification as either SINGLE (green), MULTI (blue), BOTH-Large bands
666 subset (magenta), BOTH-Mid-sized bands subset (red), or NONE (gray).

667 **Tables & Figures**

668

669 **Table 1.** Criteria used to objectively classify objects output from the MET MODE tool applied to
670 stitched regional composite reflectivity data.
671

	Length (L)	Width (W)	Aspect Ratio (W/L)
Large Band	$\geq 200 \text{ km}$	$20 \leq W \leq 100 \text{ km}$	≤ 0.5
Mid-sized Band	$< 200 \text{ km}$	$10 \leq W \leq 50 \text{ km}$	≤ 0.5
Undefined/Cell	$10 \leq L \leq 100 \text{ km}$	$10 \leq W \leq 100 \text{ km}$	> 0.5

672

673

674 **Table 2.** Case classification by band type, cyclone stage, and band motion for 6-hourly events
 675 during banded cases.
 676

Classification	Cyclone Stage	Number of Events with Band Movement Perpendicular (Parallel) to the Long Axis of the Band
Single Band Only	Developing	0 (0)
	Mature	3 (2)
Multi-bands Only	Developing	6 (12)
	Mature	14 (3)
Both Single & Multi-bands	Developing	15 (28)
	Mature	58 (6)
Non-banded	Developing	29
	Mature	17

677
 678
 679
 680

681

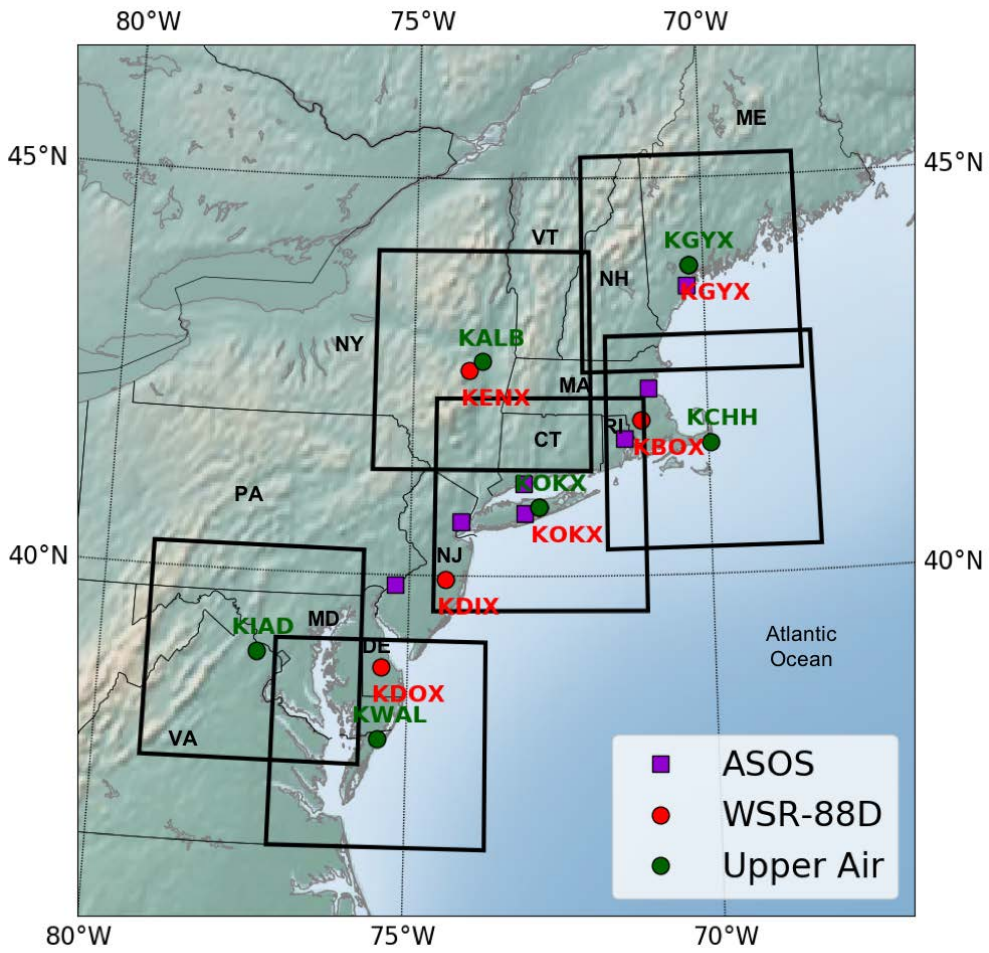
Table 3. Environmental banding ingredients for each classification type.

	700 hPa Frontogenesis (K 100 km ⁻¹ h ⁻¹)	700 hPa MPV* (PVU)	750-650 hPa $\frac{dT}{dP}$ (x 10 ⁻⁴ °C Pa ⁻¹)	750-650 hPa $\frac{d\theta_e^*}{dP}$ (x 10 ⁻⁴ K Pa ⁻¹)	950-750 hPa Wind Speed Difference (m s ⁻¹)
SINGLE	0.90	-0.77	-4.98	4.84	3.71
MULTI	0.13	-0.53	-4.71	5.04	5.84
BOTH-LARGE BANDS	0.99	-0.75	-3.08	8.04	3.01
BOTH-MID-SIZED BANDS	0.14	-0.54	-4.55	5.36	5.67
NONE	0.12	-0.63	-4.68	5.32	10.51

682

683

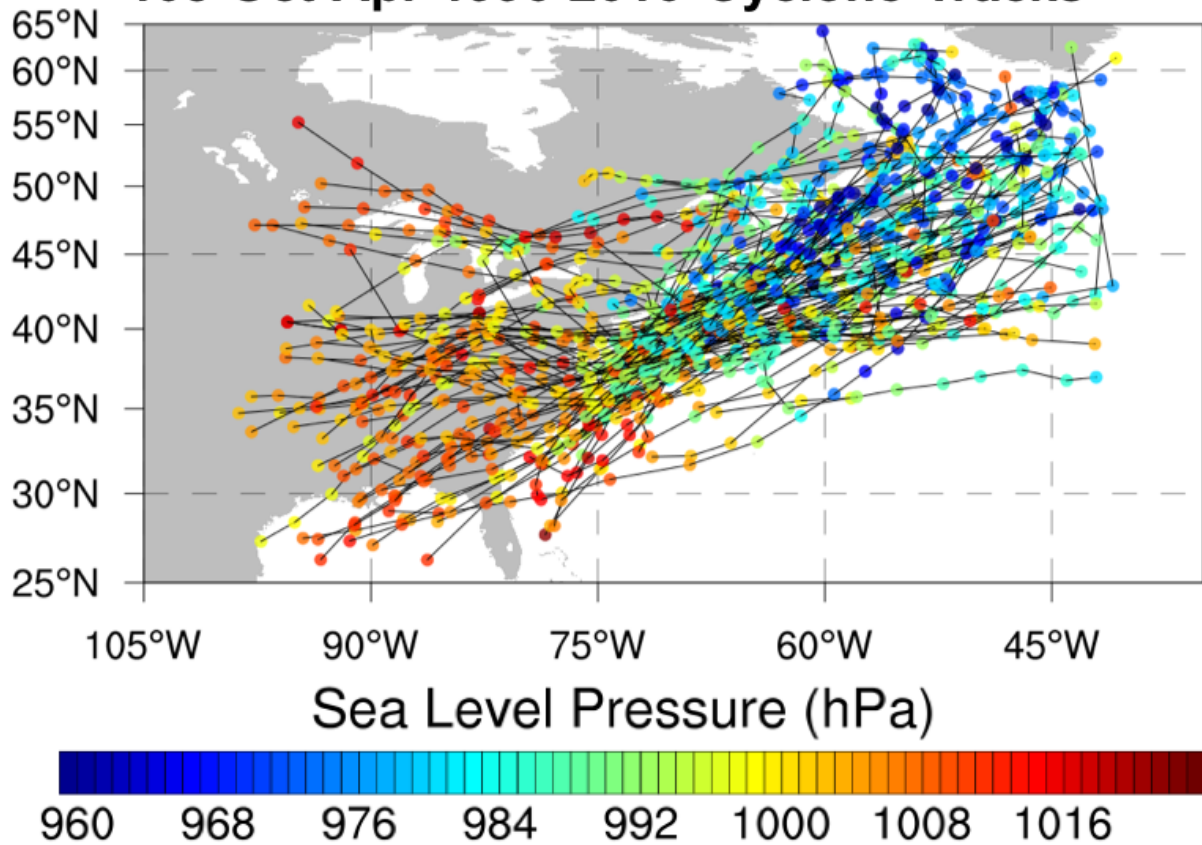
684



685
686
687
688
689
690
691

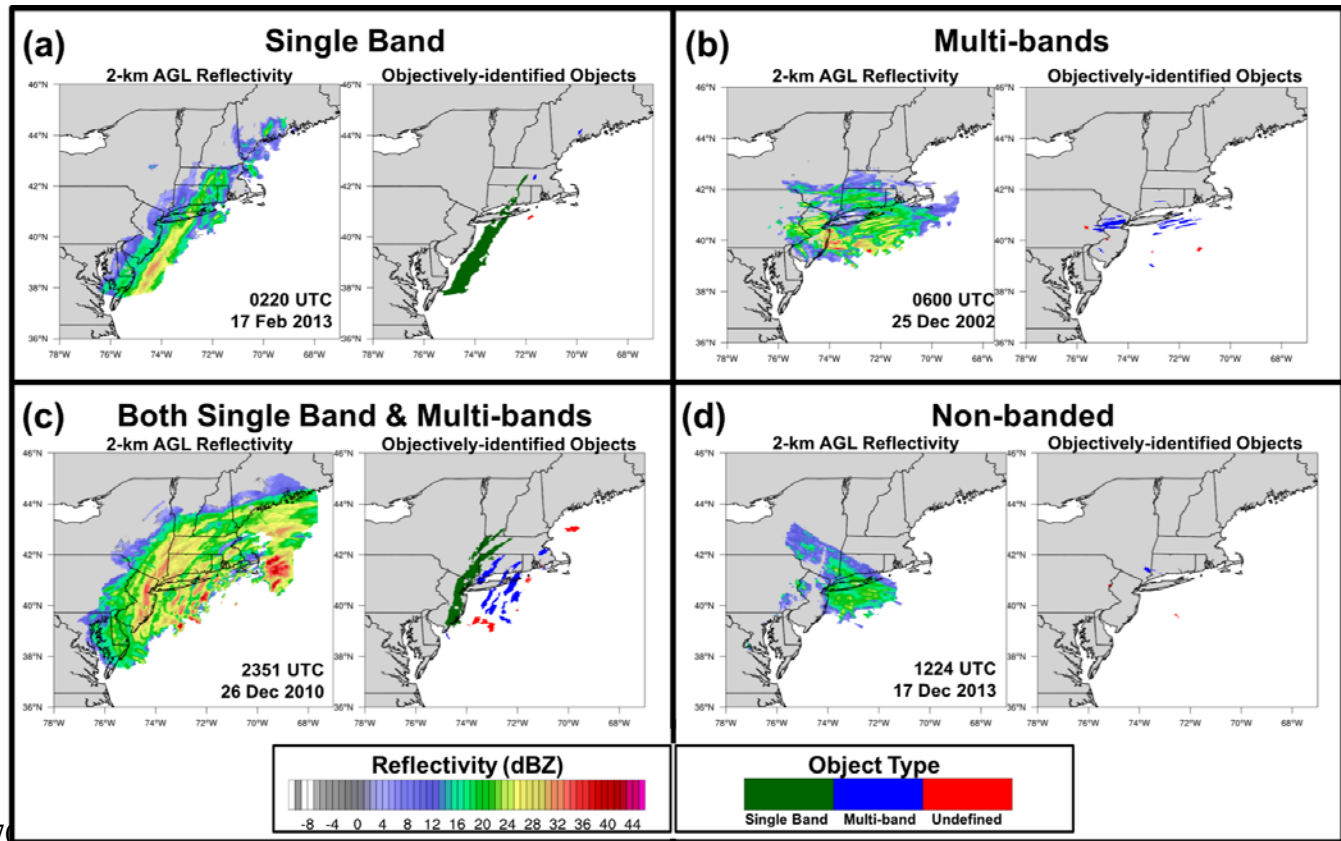
Figure 1. Map showing locations of six upper-air sites (green circles) used for vertical profiles through regional classification given by each box bounding ~150-km around the upper-air site. Locations of regional NWS WSR-88D radar (red circles) and Automated Surface Observing System (ASOS) sites (purple squares) are shown.

108 Oct-Apr 1996-2016 Cyclone Tracks



692
693

694 **Figure 2.** Sea level pressure (SLP) along each of the 108 cyclone tracks in the study with points
695 along the track colored by SLP with warmer colors indicating weaker cyclones and cooler colors
696 indicating stronger cyclones.
697
698
699
700
701

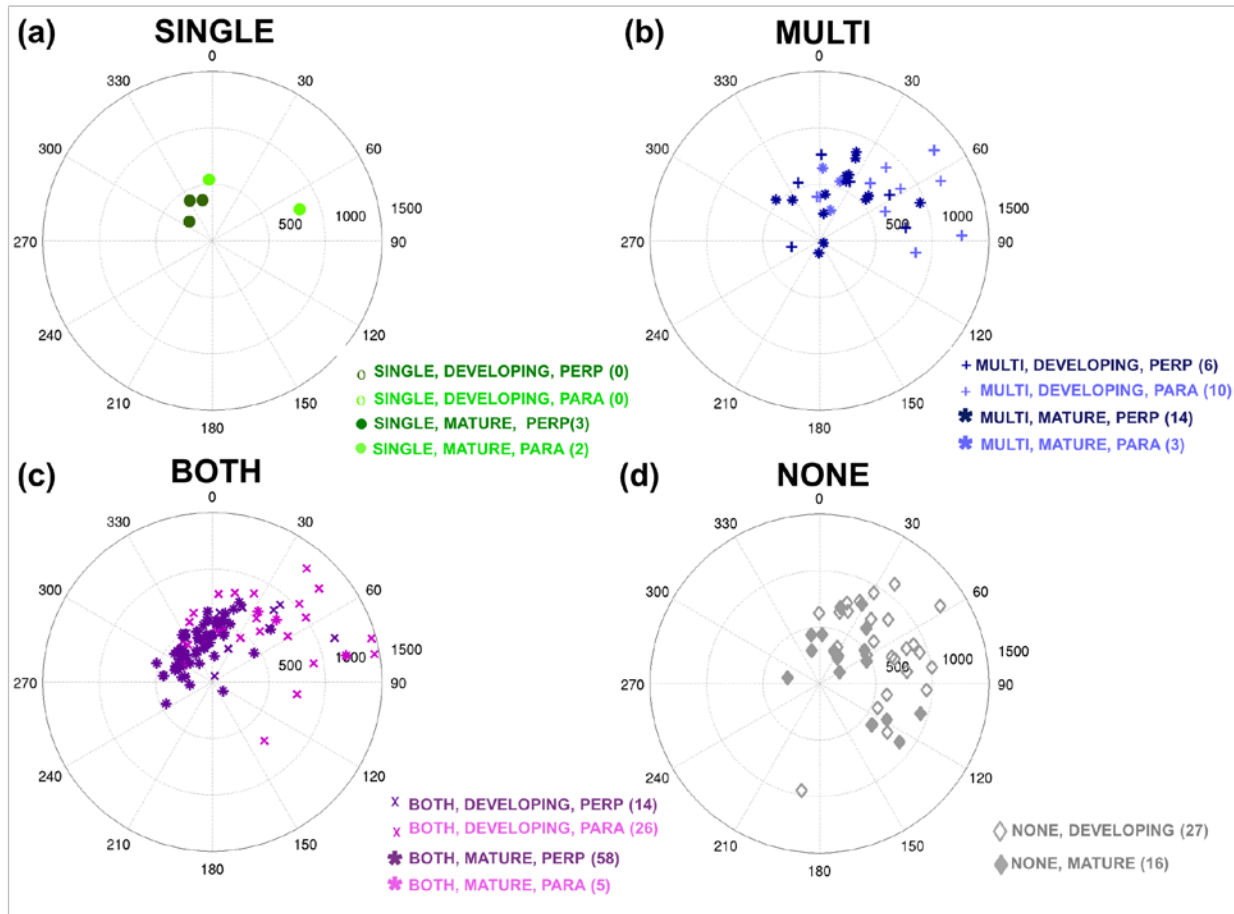


7
703

704 **Figure 3.** Examples of 2-km AGL stitched regional composite reflectivity and the resulting
 705 classified objects from the MET MODE tool output for the four banding classifications exhibited
 706 in Northeast U.S. winter storms, (a) a large, single band, (b) multi-bands, (c) both single and
 707 multi-bands, and (d) non-banded.

708
709

710

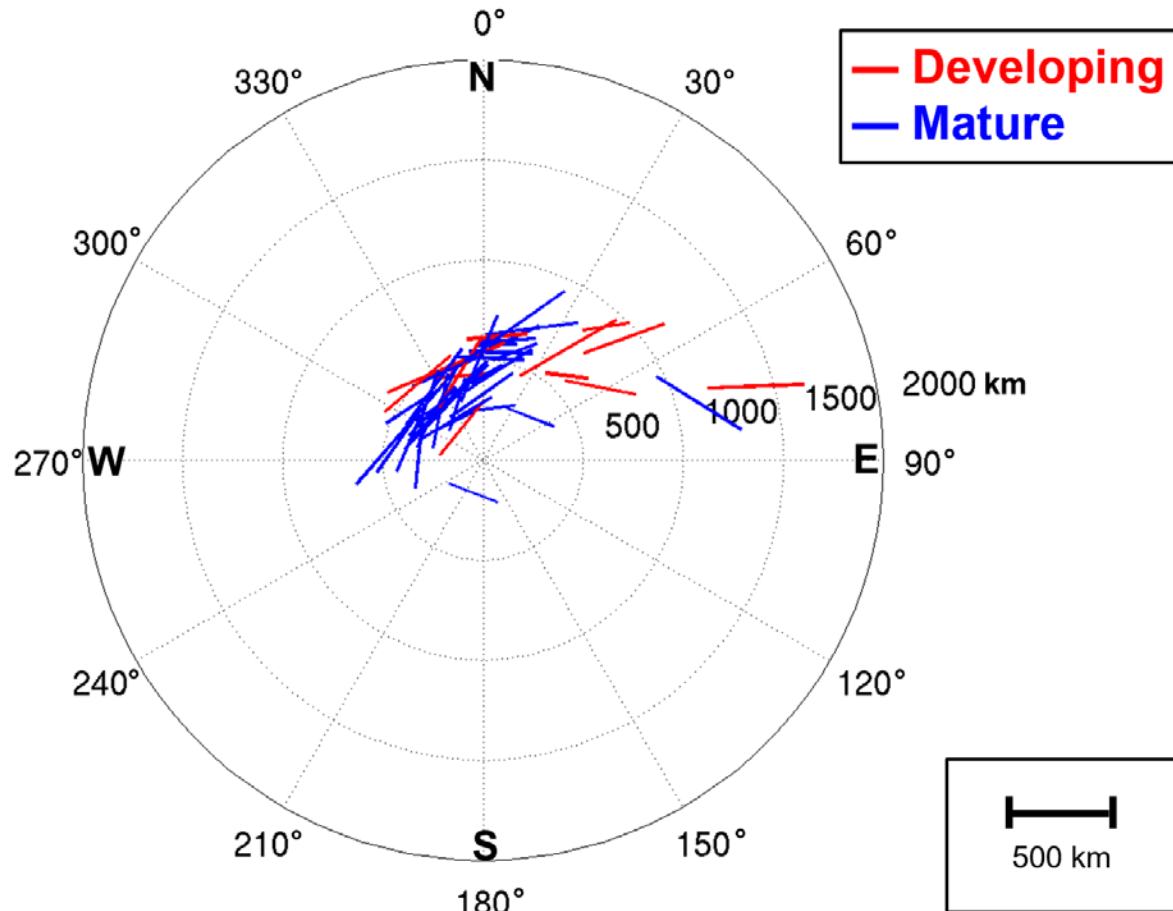


711

712

713 **Figure 4.** Distance and angle from cyclone low pressure center for 193 events for (a) SINGLE
 714 events for mature (filled circle) and developing (open circle) cyclones for parallel moving bands
 715 (light green) and perpendicular moving bands (dark green), (b) MULTI events for mature
 716 (asterisk) and developing (plus sign) cyclones for parallel moving bands (light blue) and
 717 perpendicular moving bands (dark blue), (c) BOTH events for mature (asterisk) and developing
 718 (cross) cyclones for parallel moving bands (light purple) and perpendicular moving bands (dark
 719 purple), (d) NONE events for mature (filled diamond) and developing (open diamond) cyclones.
 720 The radial distance is in kilometers and the angle from the cyclone to the sounding location at the
 721 center of the domain of the classified event is in degrees.
 722

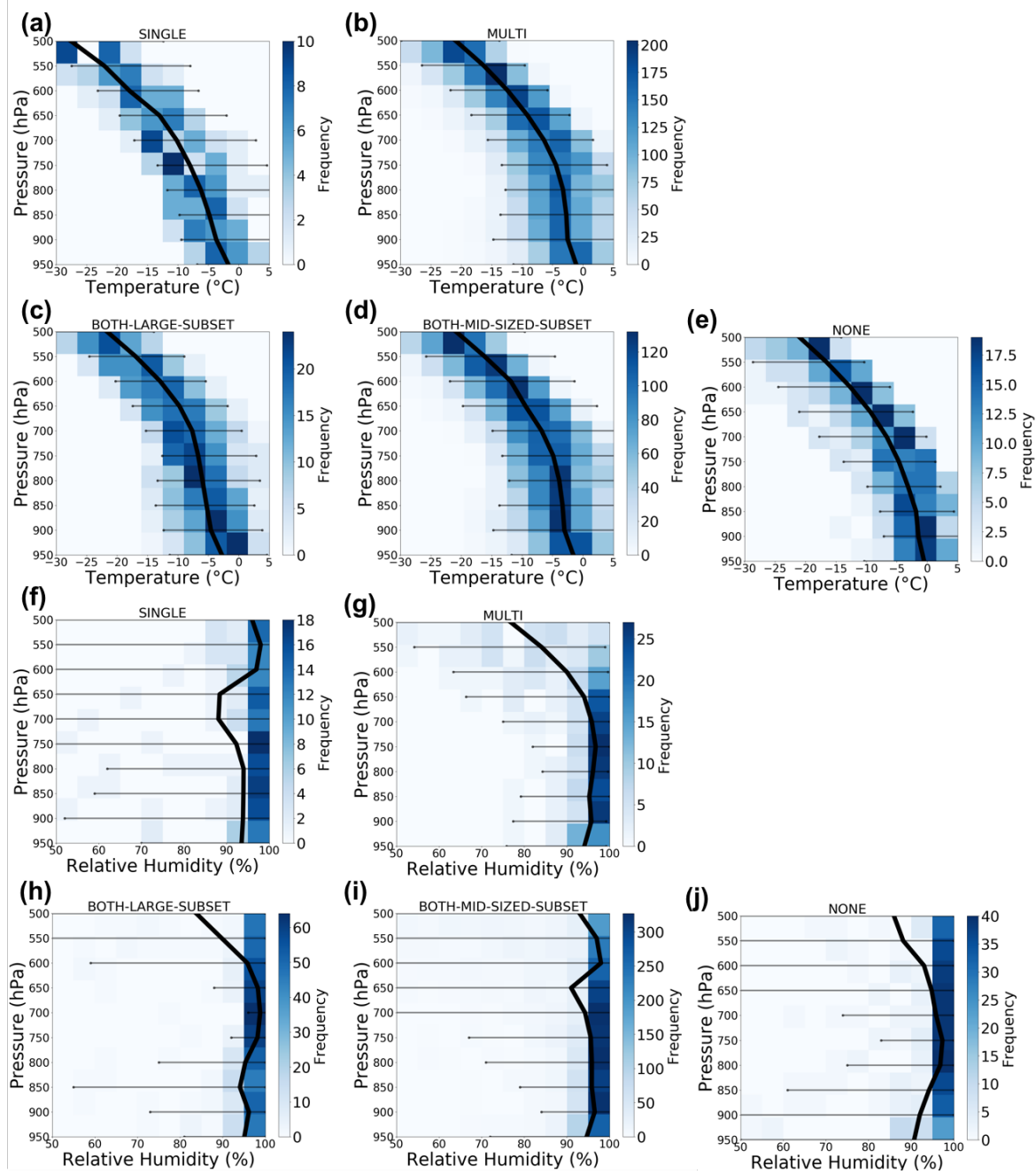
723



724
725

726 **Figure 5.** Large band locations and orientations relative to the cyclone center (origin of plot)
727 with the radius in km and angle in degrees. Bands associated with mature cyclones are in blue
728 and developing cyclones are in red.
729

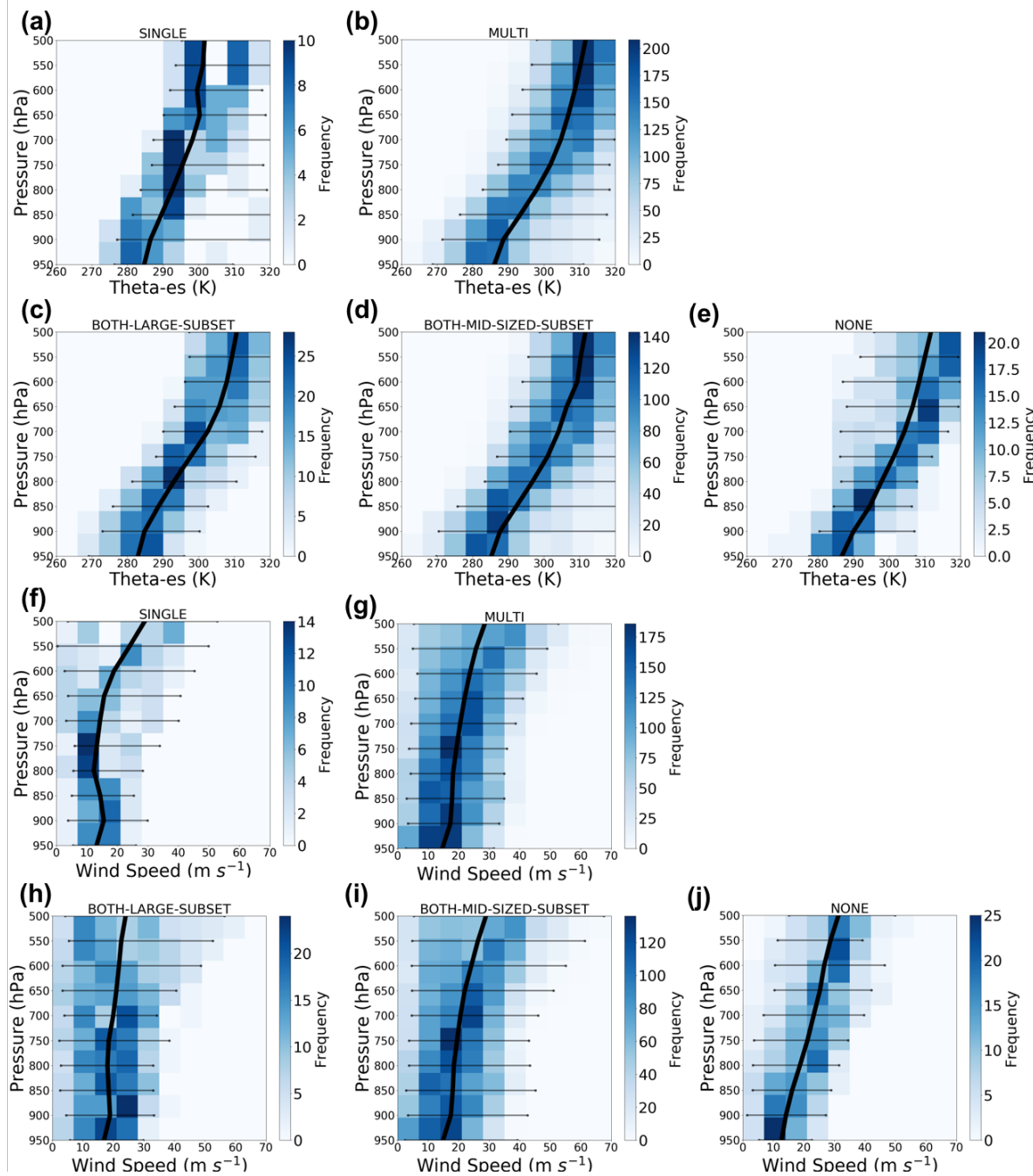
730



731
732

733 **Figure 6.** Vertical profiles of (a–e) temperature ($^{\circ}\text{C}$) and (f–j) relative humidity (%) for events
734 classified as (a,f) SINGLE, (b,g) MULTI, (c,h) BOTH-Large bands subset, (d,i) BOTH-Mid-
735 sized bands subset, (e,j) NONE events. Bold lines denote the mean profile for each classification
736 with markers indicating the 2.5th and 97.5th percentiles of the mean with 95% confidence.
737

738



739

740

741 **Figure 7.** As in Figure 6 but for (a–e) saturation equivalent potential temperature (K) and (f–j)
 742 wind speed (kts).

743

744

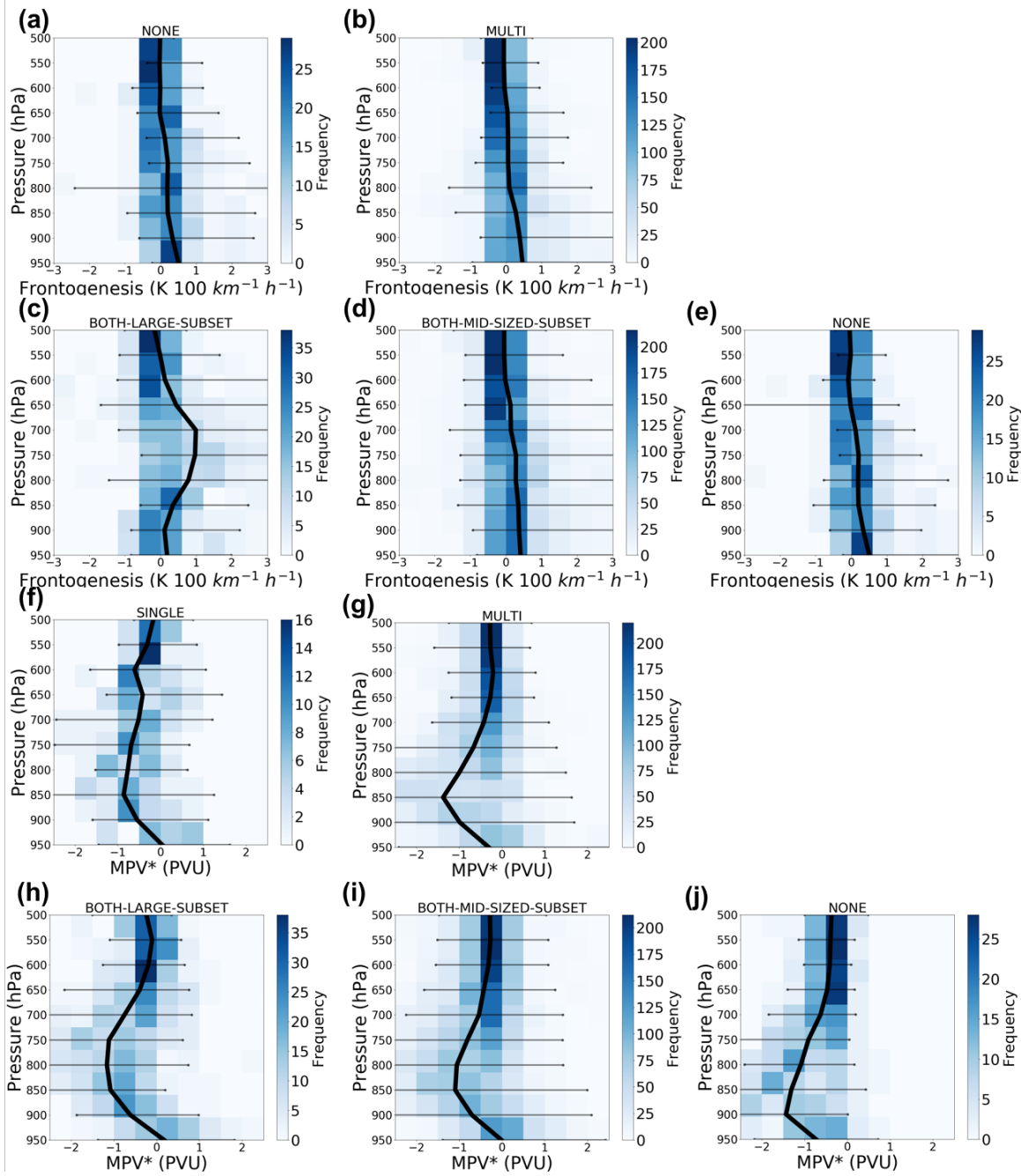
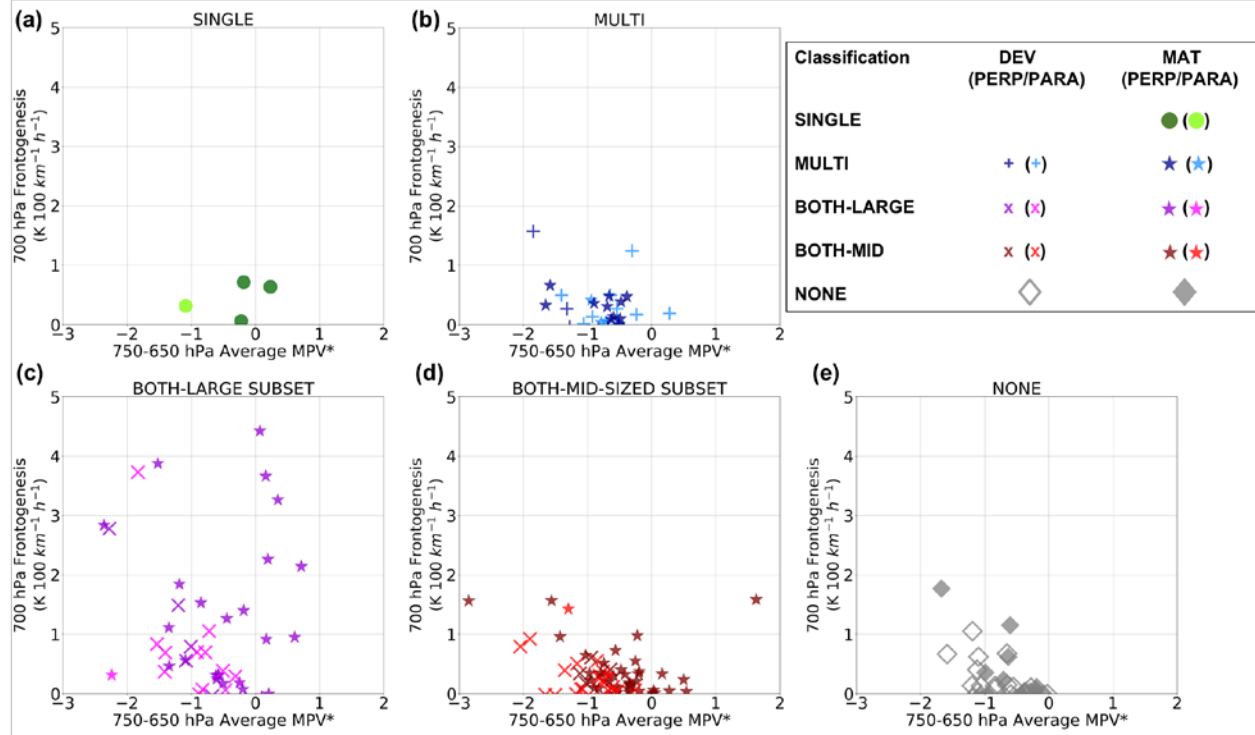


Figure 8. As in Figure 6 but for (a–e) frontogenesis ($\text{K } 100 \text{ km}^{-1} \text{ h}^{-1}$) and (f–j) saturation equivalent potential vorticity (MPV*, PVU).



753
754
755
756
757
758
759
760
761

Figure 9. The relationship between 750–650-hPa averaged saturation equivalent potential vorticity (MPV*, PVU) on the abscissa and 700-hPa frontogenesis ($\text{K } 100 \text{ km}^{-1} \text{ h}^{-1}$) on the ordinate for (a) SINGLE, (b) MULTI, (c) BOTH-Large bands subset, (d) BOTH-Mid-sized bands subset, and (e) NONE classified events from developing (DEV) or mature (MAT) cyclones exhibiting perpendicular (PERP) or parallel (PARA) band motion.

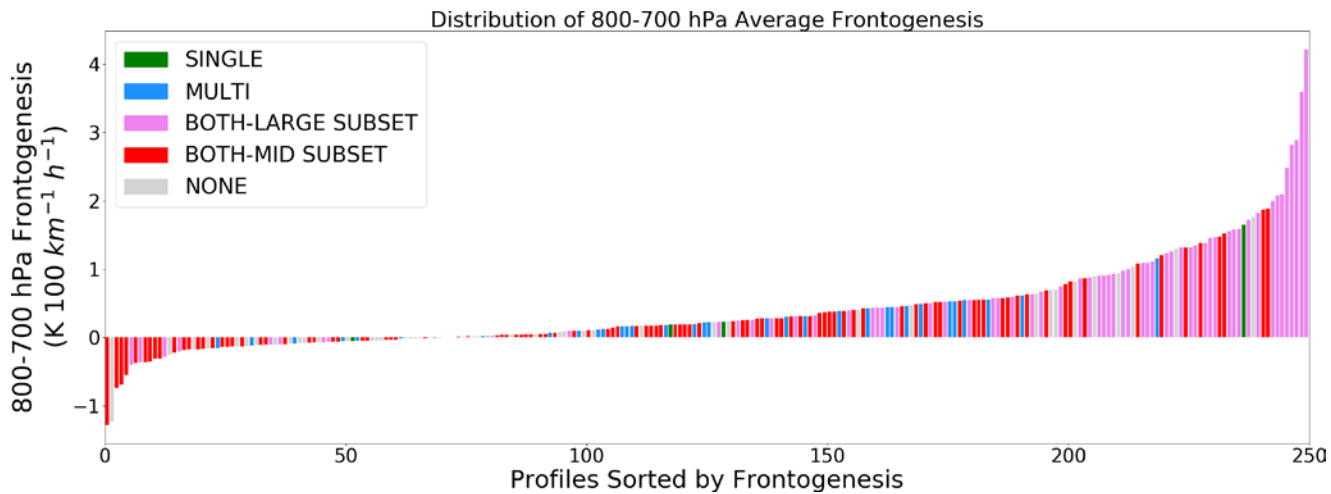


Figure 10. Distribution of 800-700-hPa average frontogenesis for all events in the dataset colored by classification as either SINGLE (green), MULTI (blue), BOTH-Large bands subset (magenta), BOTH-Mid-sized bands subset (red), or NONE (gray).

762
763
764
765
766
767
768
769
770
771
772
773
774
775
776